

# Einstein and Debye temperatures, electron-phonon coupling constant and a probable mechanism for ambient-pressure room-temperature superconductivity in intercalated graphite

Evgeny F. Talantsev<sup>1,2</sup>

<sup>1</sup>M. N. Miheev Institute of Metal Physics, Ural Branch, Russian Academy of Sciences, 18, S. Kovalevskoy St., Ekaterinburg 620108, Russia

<sup>2</sup>NANOTECH Centre, Ural Federal University, 19 Mira St., Ekaterinburg 620002, Russia

## Abstract

Recently, Ksenofontov *et al* (*arXiv:2510.03256*) observed ambient pressure room-temperature superconductivity in graphite intercalated with lithium-based alloys with transition temperature (according to magnetization measurements)  $T_c = 330\text{ K}$ . Here, I analyzed the reported temperature dependent resistivity data  $\rho(T)$  in these graphite-intercalated samples and found that  $\rho(T)$  is well described by the model of two series resistors, where each resistor is described as either an Einstein conductor or a Bloch-Grüneisen conductor. Deduced Einstein and Debye temperatures are  $\Theta_{E,1} \cong 250\text{ K}$  and  $\Theta_{E,2} \cong 1,600\text{ K}$ , and  $\Theta_{D,1} \cong 300\text{ K}$  and  $\Theta_{D,2} \cong 2,200\text{ K}$ , respectively. Following the McMillan formalism, from the deduced  $\Theta_{E,2}$  and  $\Theta_{D,2}$ , the electron-phonon coupling constant  $\lambda_{e-ph} = 2.2 - 2.6$  was obtained. This value of  $\lambda_{e-ph}$  is approximately equal to the value of  $\lambda_{e-ph}$  in highly compressed superconducting hydrides. Based on this, I can propose that the observed room-temperature superconductivity in intercalated graphite is localized in nanoscale Sr-Ca-Li metallic flakes/particles, which adopt the phonon spectrum from the surrounding bulk graphite matrix, and as a result, conventional electron-phonon superconductivity arises in these nano-flakes/particles at room temperature. Experimental data reported by Ksenofontov *et al* (*arXiv:2510.03256*) on trapped magnetic flux decay in intercalated graphite samples supports the proposition.

**Keywords:** room-temperature superconductivity; ambient pressure superconductivity; Debye temperature; electron-phonon coupling constant.

# Einstein and Debye temperatures, electron-phonon coupling constant and a probable mechanism for ambient-pressure room-temperature superconductivity in intercalated graphite

## I. Introduction

Near-room-temperature superconductivity in hydrides was experimentally discovered by Drozdov *et al.*<sup>1</sup> in highly compressed H<sub>3</sub>S. Over the past decade, the joint efforts of the high-pressure physics and first-principles calculations communities have led to the experimental discovery of dozens highly compressed hydride superconductors<sup>2–45</sup>, including the ternary hydride LaSc<sub>2</sub>H<sub>24</sub> with a zero-resistance superconducting transition temperature  $T_{c,zero}(P = 262 \text{ GPa}) = 292 \text{ K}$ <sup>46</sup>. Several new experimental techniques have been developed during this journey<sup>47–59</sup>. The exploration of this scientific *terra incognita* is continuing by first-principles calculations<sup>60–66</sup>, as well as detailed characterization of the superconducting state in highly compressed hydrides<sup>55,67–69</sup>.

While superhydrides remain the main family in which superconductivity is expected to be found at room temperature and ambient pressure<sup>60–64,70–72</sup>, Ksenofontov *et al.*<sup>73</sup> recently reported the discovery of a new class of superconductors at ambient pressure, in which the zero-field cooling (ZFC) and field cooling (FC) magnetization curves show a transition temperature up to  $T_{c,diamagnet}(P = 0.1 \text{ MPa}) = 330 \text{ K}$ . These superconductors<sup>73</sup> are the graphite intercalated with strontium-calcium-lithium alloys.

Here, in an attempt to determine fundamental superconducting properties of this new class of superconductors, I analyzed the reported temperature dependent resistivity data  $\rho(T)$  and found that  $\rho(T)$  is well described by the two-component Bloch-Grüneisen equation. Deduced Debye temperatures are  $\Theta_{D,1} = (240 - 340) \text{ K}$  and  $\Theta_{D,2} = (2,200 - 2,700) \text{ K}$ . Following advanced

McMillan formalism<sup>74–76</sup>, the Debye temperature of  $\Theta_{D,2} \cong 2,200\text{ K}$  and transition temperature of  $T_c = 330\text{ K}$  mean that the intercalated graphite has an electron-phonon coupling constant  $\lambda_{e-ph} \cong 2.15$ , which is a typical value for highly compressed near-room-temperature superconducting hydrides<sup>10,76–84</sup>.

## II. Two series resistors model

The Debye temperature  $\Theta_D$  can be derived from fitting the specific heat data  $C_p(T)$  to the Debye equation<sup>85–87</sup>:

$$C_{p,D}(T) = \gamma \times T + 9 \times R_{gc} \times N \times \left(\frac{T}{\Theta_D}\right)^3 \int_0^{\frac{\Theta_D}{T}} \frac{x^4 e^x}{(e^x - 1)^2} dx \quad (1)$$

where  $\gamma$  is the Sommerfeld coefficient,  $R_{gc} = 8.31\text{ J K}^{-1}\text{ mol}^{-1}$  is the universal gas constant.

Some research groups<sup>88</sup> utilized multichannel Debye equation proposed by Bouquet *et al.*<sup>89</sup>:

$$C_p(T) = \gamma \times T + 9 \times R_{gc} \times \sum_{i=1}^M A_i \left(\frac{T}{\Theta_{D,i}}\right)^3 \int_0^{\frac{\Theta_{D,i}}{T}} \frac{x^4 e^x}{(e^x - 1)^2} dx \quad (2)$$

where  $A_i$  are constants (depended from given crystalline structure and chemical composition),  $M$  is a number of the channels for the Debye modes.

Wälti *et al.*<sup>90</sup> proposed a combined Debye-Einstein model, which is also in use<sup>91,92</sup>:

$$C_p(T) = \gamma \times T + \alpha \times C_{p,D}(T) + (1 - \alpha) \times C_{p,E}(T) \quad (3)$$

where the third term represents the optical phonon-mode contributions and it is described by Einstein equation for heat capacity:

$$C_{p,E}(T) = 3 \times R_{gc} \times \left(\frac{\Theta_E}{T}\right)^2 \frac{e^{\left(\frac{\Theta_E}{T}\right)}}{\left(e^{\left(\frac{\Theta_E}{T}\right)} - 1\right)^2} \quad (4)$$

For multichannel case, Eq. 3 can be rewritten as following:

$$C_p(T) = \gamma \times T + 9 \times R_{gc} \times \sum_{i=1}^M A_i \left( \frac{T}{\Theta_{D,i}} \right)^3 \int_0^{\frac{\Theta_{D,i}}{T}} \frac{x^4 e^x}{(e^x - 1)^2} dx + 3 \times R_{gc} \times \sum_{j=1}^P B_j \left( \frac{\Theta_{E,j}}{T} \right)^2 \frac{e^{\left( \frac{\Theta_{E,j}}{T} \right)}}{\left( e^{\left( \frac{\Theta_{E,j}}{T} \right)} - 1 \right)^2} \quad (5)$$

where  $A_i$  and  $B_j$  are constants,  $M$  and  $P$  are number of the channels for the Debye modes and the Einstein modes, respectively;  $\Theta_{D,i}$  is the Debye temperature of the  $i$ -channel,  $\Theta_{E,j}$  is the Einstein temperature of the  $j$ -channel.

The Debye temperature  $\Theta_D$  can also be derived from fitting temperature-dependent resistivity  $\rho(T)$  to the Bloch-Grüneisen<sup>93,94</sup> equation (where the Debye temperature,  $\Theta_D$ , is one of free-fitting parameters):

$$\rho(T) = \rho_0 + A \times \left( \frac{T}{\Theta_D} \right)^5 \times \int_0^{\frac{\Theta_D}{T}} \frac{x^5}{(e^x - 1)(1 - e^{-x})} dx \quad (6)$$

where  $\rho_0$ , and  $A$  other are free-fitting parameters. Eq. 6 is one of the approaches to determine the Debye temperature from experimental data<sup>76–78,92,95–103</sup>. Wiesmann *et al*<sup>104</sup> advanced this model by assuming that there is an additional conduction channel with a temperature-independent resistance  $R_{sat}$  that is connected in parallel with the resistor described by Equation 1:

$$\frac{1}{\rho(T)} = \frac{1}{\rho_{sat}} + \frac{1}{\rho_0 + A \times \left( \frac{T}{\Theta_D} \right)^5 \times \int_0^{\frac{\Theta_D}{T}} \frac{x^5}{(e^x - 1)(1 - e^{-x})} dx} \quad (2)$$

Based on the Matthiessen rule, Varshney<sup>105</sup> proposed an alternative model for the  $\rho(T)$  in MgB<sub>2</sub>. This model is based on the assumption (which is similar to one made in Ref.<sup>90</sup>) that the phonon spectrum consists of two parts: an acoustic branch of the Debye type (which is characterized by the Debye temperature  $\Theta_D$ ) and an optical mode with characteristic Einstein temperature,  $\Theta_E$ . In the result, the proposed equation<sup>105</sup> is:

$$\rho(T) = \rho_0 + A \times \left( \frac{T}{\Theta_D} \right)^5 \times \int_0^{\frac{\Theta_D}{T}} \frac{x^5}{(e^x - 1)(1 - e^{-x})} dx + B \times \frac{\frac{\Theta_E^2}{T}}{\left( e^{\frac{\Theta_E}{T}} - 1 \right) \left( 1 - e^{-\frac{\Theta_E}{T}} \right)} \quad (9)$$

where the third term is the Einstein resistivity model<sup>106,107</sup>, and  $\rho_0$ ,  $A$ ,  $\Theta_D$ ,  $B$ ,  $\Theta_E$  are free fitting parameters.

Because there is no additional information on the phonon spectrum in the intercalated graphite, I employed three two-series resistances models to fit the  $\rho(T)$  data reported by Ksenofontov *et al.*<sup>73</sup> for graphite intercalated with lithium-based alloys:

$$\rho(T) = \rho_0 + \sum_{i=1}^2 A_i \times \left( \frac{T}{\Theta_{D,i}} \right)^5 \times \int_0^{\frac{\Theta_{D,i}}{T}} \frac{x^5}{(e^x - 1)(1 - e^{-x})} dx \quad (10)$$

this model is designated as the 2BG model, where  $\rho_0$ ,  $A_i$ ,  $\Theta_{D,i}$  are free-fitting parameters;

$$\rho(T) = \rho_0 + \sum_{i=1}^2 B_i \times \frac{\frac{\Theta_{E,i}^2}{T}}{\left( e^{\frac{\Theta_{E,i}}{T}} - 1 \right) \left( 1 - e^{-\frac{\Theta_{E,i}}{T}} \right)} \quad (11)$$

this model is designated as the 2E model, where  $\rho_0$ ,  $B_i$ ,  $\Theta_{E,i}$  are free-fitting parameters; and Eq. 9 is designated as the BGE model.

### III. Einstein and Debye temperatures in intercalated graphite samples

**Sample I** (in the report by Ksenofontov *et al.*<sup>73</sup>) is Li-intercalated graphite sample. Figure 1 shows fits of the  $\rho(T)$  data for this sample **Sample I**<sup>73</sup> to three models (Eqs. 9-11). Deduced characteristic temperatures and temperature dependent contributions of each term are shown in each panel of Fig. 1. The derived temperatures  $\Theta_E$ ,  $\Theta_{E,2}$ , and  $\Theta_{D,2}$  are approximately in the same range with the Debye temperature in graphene<sup>108–111</sup>  $\Theta_D \cong (1,700 - 2300) K$ . At the same time,  $\Theta_D$ ,  $\Theta_{E,1}$ , and  $\Theta_{D,1}$  are close to the reported in-plane<sup>112</sup> Debye temperature in the  $\text{LiC}_n$  ( $n = 6, 12$ )  $\Theta_{D,\parallel} \cong 350 K$ .

**Sample IIId** (in the report by Ksenofontov *et al.*<sup>73</sup>) is Sr-Ca-Li-intercalated graphite sample, which showed the diamagnetic superconducting transition  $T_{c,dia} = 330 K$ . Figure 2 shows fits of the  $\rho(T)$  data for this sample **Sample IIId**<sup>73</sup> to three models (Eqs. 9-11).

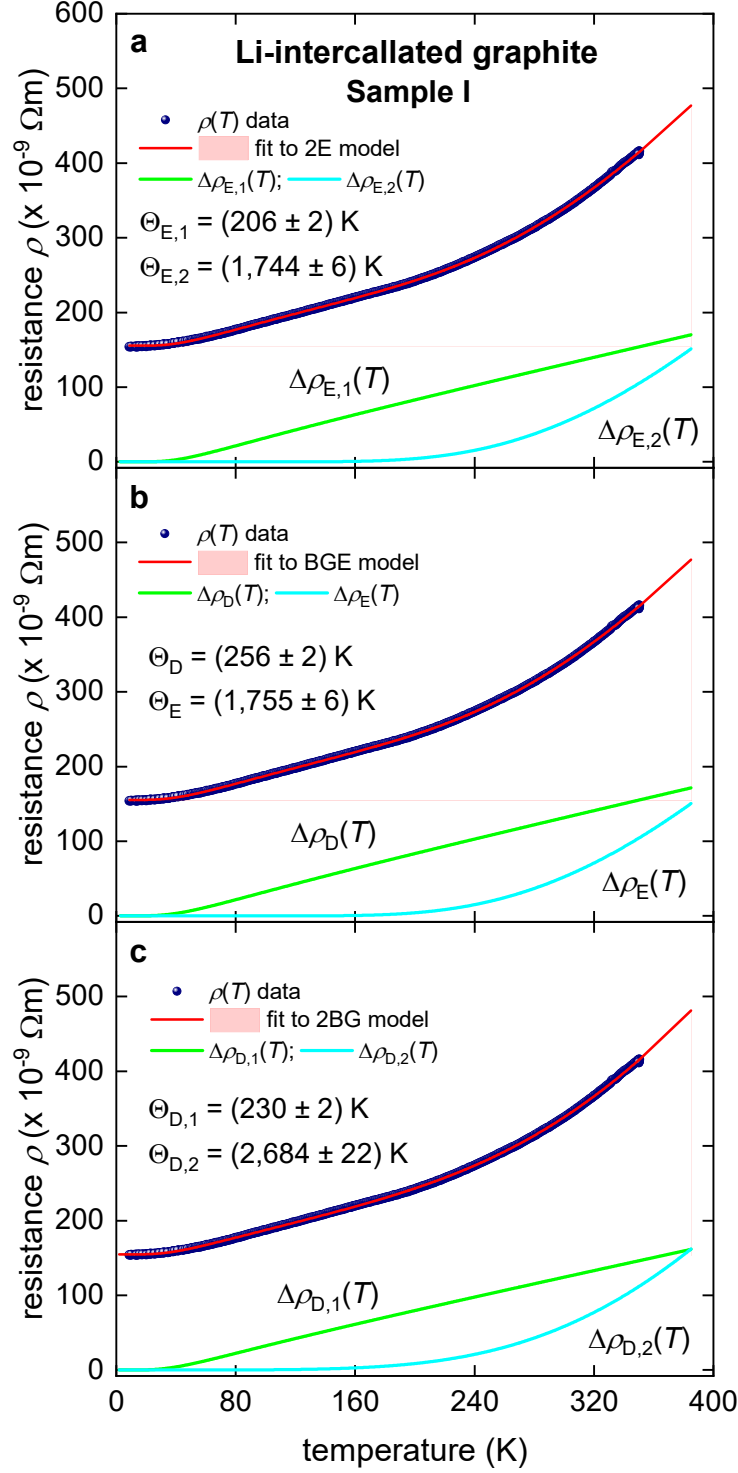


**Figure 1.**  $\rho(T, B = 0)$  of the graphite intercalated with lithium (**Sample I**<sup>73</sup> fabricated and measured by Ksenofontov et al.<sup>73</sup>) and fits to (a) double Einstein model (Eq. 11, the goodness of fit  $R$ -square COD = 0.99992); (b) combined Bloch-Grüneisen and Einstein model<sup>105</sup> (Eq. 9, the goodness of fit is 0.99993); and (c) double Bloch-Grüneisen model (Eq. 10, the goodness of fit is COD = 0.99991). The thickness of 95% confidence bands (pink shadow areas) is narrower than the width of the fitting lines.

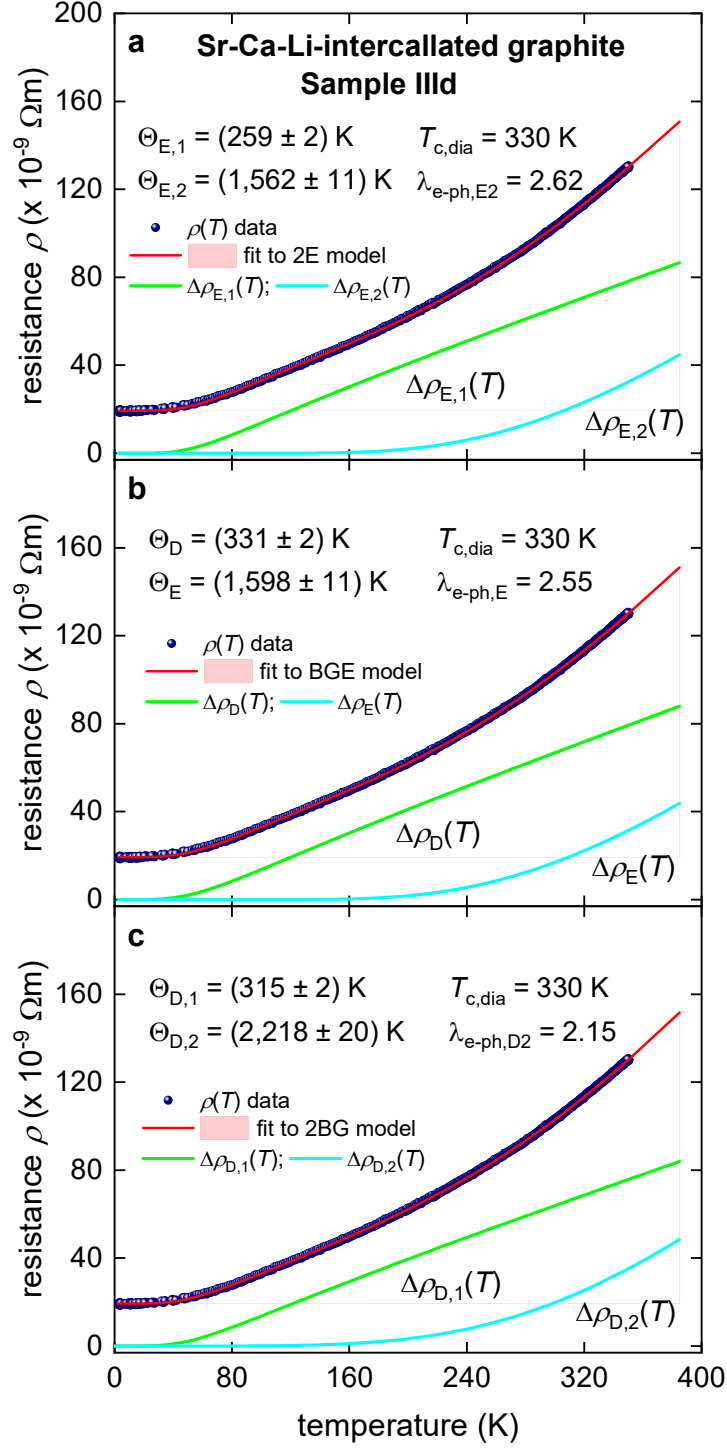


**Figure 1.**  $\rho(T, B = 0)$  of the graphite intercalated with strontium-calcium-lithium alloy (**Sample IIIId**<sup>73</sup> fabricated and measured by Ksenofontov et al.<sup>73</sup>) and fits to (a) double Einstein model (Eq. 11, the goodness of fit  $R$ -square COD = 0.99993); (b) combined Bloch-Grüneisen and Einstein model<sup>105</sup> (Eq. 9, the goodness of fit is 0.99994); and (c) double Bloch-Grüneisen model (Eq. 10, the goodness of fit is COD = 0.99996). The thickness of 95% confidence bands (pink shadow areas) is narrower than the width of the fitting lines.

Deduced characteristic temperatures and temperature dependent contributions of each term are shown in each panel of Fig. 2. The derived  $\Theta_{E,i}$  and  $\Theta_{D,i}$  values are within the same ballpark range as the values deduced in Li-intercalated graphite (**Sample I**, Fig. 1).

#### IV. Electron-phonon coupling constant in room temperature superconductor Sr-Ca-Li-graphite

Deduced Einstein and Debye temperatures can be used to derive the electron-phonon coupling constant  $\lambda_{e-ph}$ , because the latter is the root of the advanced McMillan equations<sup>67,74–76,113</sup>:

$$\begin{cases} T_c = \frac{\Theta_E}{1.20} \times e^{-\left(\frac{1.04(1+\lambda_{e-ph,E})}{\lambda_{e-ph,E}-\mu^* \times (1+0.62 \times \lambda_{e-ph,E})}\right)} \times f_1 \times f_2^* \\ f_1 = \left(1 + \left(\frac{\lambda_{e-ph,E}}{2.46 \times (1+3.8 \times \mu^*)}\right)^{3/2}\right)^{1/3} \\ f_2^* = 1 + (0.0241 - 0.0735 \times \mu^*) \times \lambda_{e-ph,E}^2 \end{cases} \quad (12)$$

and

$$\begin{cases} T_c = \frac{\Theta_D}{1.45} \times e^{-\left(\frac{1.04(1+\lambda_{e-ph,D})}{\lambda_{e-ph,D}-\mu^* \times (1+0.62 \times \lambda_{e-ph,D})}\right)} \times f_1 \times f_2^* \\ f_1 = \left(1 + \left(\frac{\lambda_{e-ph,D}}{2.46 \times (1+3.8 \times \mu^*)}\right)^{3/2}\right)^{1/3} \\ f_2^* = 1 + (0.0241 - 0.0735 \times \mu^*) \times \lambda_{e-ph,D}^2 \end{cases} \quad (13)$$

where  $\mu^*$  is the Coulomb pseudopotential parameter (ranging within<sup>114</sup>  $\mu^* = 0.10 - 0.15$ ). In Figure 2, the derived  $\lambda_{e-ph,E}$  and  $\lambda_{e-ph,D}$  values were calculated in the assumption of  $\mu^* = 0.10$ .

#### V. Discussion

Based on results reported by Ksenofontov *et al.*<sup>73</sup> and results reported above, I can hypothesize that the observed room-temperature superconductivity in intercalated graphite is localized in nanoscale Sr-Ca-Li metallic flakes/particles, which cannot exhibit their own phonon



spectrum and thus receive the phonon spectrum from the surrounding graphite matrix (with Einstein temperature  $\Theta_{E,2} \cong 1,600 \text{ K}$ , or Debye temperature  $\Theta_{D,2} \cong 2,500 \text{ K}$ ). Such high  $\Theta_E$  and  $\Theta_D$  bust superconducting transition temperature  $T_c$  within electron-phonon phenomenology<sup>74,75,113,115,116</sup> (Eqs. 12,13).

In addition to these high  $\Theta_E$  and  $\Theta_D$ , intercalated graphite has a prominent low frequency part of the phonon spectrum with  $\Theta_{E,1} \cong 250 \text{ K}$  or  $\Theta_{D,1} \cong 350 \text{ K}$ , which boosts the electron-phonon coupling constant  $\lambda_{e-ph}$ :

$$\lambda_{e-ph} = 2 \times \int_0^\infty \frac{\alpha^2(\omega) \times F(\omega)}{\omega} d\omega \quad (14)$$

where  $\omega$  is the phonon frequency,  $F(\omega)$  is the phonon density of states, and  $\alpha^2(\omega) \times F(\omega)$  is the electron-phonon spectral function (more details can be found elsewhere<sup>74,75,113,114,116</sup>).

Thus, combined action of low- and high-frequency phonons causes the emergence of room-temperature superconductivity in nano-flakes/particles, because these objects cannot maintain their own phonon spectrum, and they adopt the spectrum from the surrounding graphite matrix.

Further confirmation of this hypothesis is the fact that superconducting diamagnetism is observed in  $\sim 0.1\%$  of the sample volume, which can be explained by the assumption that the superconducting phase is nanoscale flakes/particles dispersed throughout the sample volume. Small flakes/particles cannot have their independent phonon spectrum from surrounding graphite matrix, and, therefore, the flakes/particles more or less adopt the phonon spectrum of the graphite. Thus, the emergence of superconductivity in these nanoscale flakes/particles depends on the match between the phonon spectrum of the graphite, density of states at the Fermi level of the flakes/particles, etc.

In overall, the superconducting state in these nano-flakes/particles can be detected by magnetic measurements (by ZFC and FC protocols), but because of the small volume fraction of

these nano-flakes/particles ( $\sim 0.1\%$ ), the percolation path<sup>117,118</sup> cannot be formed, and thus, the resistance measurements  $R(T)$  will not show the zero-resistance state in the intercalated graphite.

Additional support for this model can be found in time-dependent magnetic measurements of the trapped magnetic flux in intercalated graphite,  $m_{trap}(T)$ . Truly, each nano-flake/particle exhibits room-temperature superconductivity, and, thus, integrated trapped magnetic flux of the sample should exhibit the logarithmic time dependence<sup>119–123</sup>. And exact this dependence was demonstrated by Ksenofontov *et al.*<sup>73</sup> (in their Fig. 4<sup>73</sup>).  $m_{trap}(T)$  data fit to the logarithmic time dependence<sup>119–123</sup> showed that the decay rate is  $S = 0.005 - 0.013$ <sup>73</sup>, which is in a ballpark of typical values for other high-temperature superconductors<sup>119–126</sup>.

#### 4. Conclusions

In this paper, I analyze recently reported data<sup>73</sup> on  $\rho(T)$  measured in an ambient-pressure room-temperature superconductor Li- and Sr-Ca-Li-intercalated graphite. The experimental data on  $\rho(T)$  are well described by the model of two series resistors, and the derived values of the Einstein and Debye temperatures allow us to calculate the electron-phonon coupling constant in intercalated Sr-Ca-Li graphite:  $\lambda_{e-ph,D} \cong 2.2$ . The obtained value is typical for highly compressed hydride superconductors<sup>10</sup>. Based on the currently available data, I propose a probable mechanism for the emergence of room-temperature superconductivity in ambient-pressure intercalated graphite.

#### Acknowledgements

The author thanks Dr. V. Ksenofontov (Max Planck Institute for Chemistry, Mainz, Germany) and all co-workers of the original study<sup>73</sup> for providing raw experimental  $\rho(T)$  data for the

analysis. The work was carried out within the framework of the state assignment of the Ministry of Science and Higher Education of the Russian Federation for the IMP UB RAS. The author gratefully acknowledged the research funding from the Ministry of Science and Higher Education of the Russian Federation under Ural Federal University Program of Development within the Priority-2030 Program.

## References

1. Drozdov, A. P., Erements, M. I., Troyan, I. A., Ksenofontov, V. & Shylin, S. I. Conventional superconductivity at 203 kelvin at high pressures in the sulfur hydride system. *Nature* **525**, 73–76 (2015).
2. Liu, H., Naumov, I. I., Hoffmann, R., Ashcroft, N. W. & Hemley, R. J. Potential high-  $T_c$  superconducting lanthanum and yttrium hydrides at high pressure. *Proceedings of the National Academy of Sciences* **114**, 6990–6995 (2017).
3. Drozdov, A. P. *et al.* Superconductivity at 250 K in lanthanum hydride under high pressures. *Nature* **569**, 528–531 (2019).
4. Somayazulu, M. *et al.* Evidence for Superconductivity above 260 K in Lanthanum Superhydride at Megabar Pressures. *Phys Rev Lett* **122**, 027001 (2019).
5. He, X.-L. *et al.* Predicted hot superconductivity in  $\text{LaSc}_2\text{H}_{24}$  under pressure. *Proceedings of the National Academy of Sciences* **121**, (2024).
6. Minkov, V. S., Prakapenka, V. B., Greenberg, E. & Erements, M. I. A Boosted Critical Temperature of 166 K in Superconducting  $\text{D}_3\text{S}$  Synthesized from Elemental Sulfur and Hydrogen. *Angewandte Chemie* **132**, 19132–19136 (2020).
7. Sun, D. *et al.* High-temperature superconductivity on the verge of a structural instability in lanthanum superhydride. *Nat Commun* **12**, 6863 (2021).
8. Cai, W. *et al.* Superconductivity above 180 K in Ca-Mg Ternary Superhydrides at Megabar Pressures. <http://arxiv.org/abs/2312.06090> (2023).
9. Kong, P. *et al.* Superconductivity up to 243 K in the yttrium-hydrogen system under high pressure. *Nat Commun* **12**, 5075 (2021).
10. Lilia, B. *et al.* The 2021 room-temperature superconductivity roadmap. *Journal of Physics: Condensed Matter* **34**, 183002 (2022).
11. Drozdov, A. P., Erements, M. I. & Troyan, I. A. Superconductivity above 100 K in  $\text{PH}_3$  at high pressures. <http://arxiv.org/abs/1508.06224> (2015).

12. Chen, W. *et al.* High-Temperature Superconducting Phases in Cerium Superhydride with a  $T_c$  up to 115 K below a Pressure of 1 Megabar. *Phys Rev Lett* **127**, 117001 (2021).
13. Troyan, I. A., Semenok, D. V., Sadakov, A. V., Lyubutin, I. . S. & Pudalov, V. M. PROGRESS, PROBLEMY I PERSPEKTIVY KOMNATNO-TEMPERATURNY SVERKhPROVODIMOSTI. *Žurnal èksperimental'noj i teoretičeskoj fiziki* **166**, 74–88 (2024).
14. Chen, W. *et al.* Enhancement of superconducting properties in the La–Ce–H system at moderate pressures. *Nat Commun* **14**, 2660 (2023).
15. Zhou, D. *et al.* Superconducting praseodymium superhydrides. *Sci Adv* **6**, 1–9 (2020).
16. Guo, J. *et al.* Unusual metallic state in superconducting A15-type La<sub>4</sub>H<sub>23</sub>. *Natl Sci Rev* <https://doi.org/10.1093/nsr/nwae149> (2024) doi:10.1093/nsr/nwae149.
17. Semenok, D. V. *et al.* Superconductivity at 161 K in thorium hydride ThH<sub>10</sub>: Synthesis and properties. *Materials Today* **33**, 36–44 (2020).
18. Troyan, I. A. *et al.* High-temperature superconductivity in hydrides. *Physics-Uspexhi* **65**, 748–761 (2022).
19. Chen, W. *et al.* Synthesis of molecular metallic barium superhydride: pseudocubic BaH<sub>12</sub>. *Nat Commun* **12**, 1–9 (2021).
20. Guo, J. *et al.* Soft superconductivity in covalent bismuth dihydride BiH<sub>5</sub>\_2\$ under extreme conditions. <http://arxiv.org/abs/2505.12062> (2025).
21. Troyan, I. A. *et al.* Non-Fermi-Liquid Behavior of Superconducting SnH<sub>4</sub>. *Advanced Science* **10**, (2023).
22. Semenok, D. V. *et al.* Superconductivity at 253 K in lanthanum–yttrium ternary hydrides. *Materials Today* **48**, 18–28 (2021).
23. Troyan, I. A. *et al.* Anomalous High-Temperature Superconductivity in YH<sub>6</sub>. *Advanced Materials* **33**, 2006832 (2021).
24. Semenok, D. V. *et al.* Effect of Magnetic Impurities on Superconductivity in LaH<sub>10</sub>. *Advanced Materials* **34**, 2204038 (2022).
25. Song, Y. *et al.* Stoichiometric Ternary Superhydride LaBeH<sub>8</sub> as a New Template for High-Temperature Superconductivity at 110 K under 80 GPa. *Phys Rev Lett* **130**, 266001 (2023).
26. Ma, C. *et al.* Synthesis of medium-entropy alloy superhydride  $\langle \text{La}, \text{Y}, \text{Ce} \rangle \text{H}_{10 \pm x}$  with high-temperature superconductivity under high pressure. *Phys Rev B* **111**, 024505 (2025).
27. Bi, J. *et al.* Giant enhancement of superconducting critical temperature in substitutional alloy (La,Ce)H<sub>9</sub>. *Nat Commun* **13**, 5952 (2022).

28. Duan, D. *et al.* Pressure-induced metallization of dense (H<sub>2</sub>S)<sub>2</sub>H<sub>2</sub> with high-T<sub>c</sub> superconductivity. *Sci Rep* **4**, 6968 (2014).
29. Song, X. *et al.* Superconductivity above 105 K in Nonclathrate Ternary Lanthanum Borohydride below Megabar Pressure. *J Am Chem Soc* **146**, 13797–13804 (2024).
30. Ma, L. *et al.* High-Temperature Superconducting Phase in Clathrate Calcium Hydride CaH<sub>6</sub> up to 215 K at a Pressure of 172 GPa. *Phys Rev Lett* **128**, 167001 (2022).
31. Sun, Y., Lv, J., Xie, Y., Liu, H. & Ma, Y. Route to a Superconducting Phase above Room Temperature in Electron-Doped Hydride Compounds under High Pressure. *Phys Rev Lett* **123**, 097001 (2019).
32. Bi, J. *et al.* Stabilization of superconductive La–Y alloy superhydride with T<sub>c</sub> above 90 K at megabar pressure. *Materials Today Physics* **28**, 100840 (2022).
33. He, X. *et al.* Superconductivity discovered in niobium polyhydride at high pressures. *Materials Today Physics* **40**, 101298 (2024).
34. Wang, Y. *et al.* Synthesis and superconductivity in yttrium superhydrides under high pressure. *Chinese Physics B* **31**, 106201 (2022).
35. Li, X. *et al.* Polyhydride CeH<sub>9</sub> with an atomic-like hydrogen clathrate structure. *Nat Commun* **10**, 3461 (2019).
36. Hong, F. *et al.* Possible superconductivity at ~70 K in tin hydride SnH<sub>x</sub> under high pressure. *Materials Today Physics* **22**, 100596 (2022).
37. Salke, N. P. *et al.* Synthesis of clathrate cerium superhydride CeH<sub>9</sub> at 80-100 GPa with atomic hydrogen sublattice. *Nat Commun* **10**, 4453 (2019).
38. Zhang, C. L. *et al.* Superconductivity above 80 K in polyhydrides of hafnium. *Materials Today Physics* **27**, 100826 (2022).
39. Shan, P. *et al.* Molecular Hydride Superconductor BiH<sub>4</sub> with T<sub>c</sub> up to 91 K at 170 GPa. *J Am Chem Soc* **147**, 4375–4381 (2025).
40. Huang, G. *et al.* Synthesis of superconducting phase of La<sub>0.5</sub>Ce<sub>0.5</sub>H<sub>10</sub> at high pressures. *Journal of Physics: Condensed Matter* **36**, 075702 (2024).
41. Chen, L.-C. *et al.* Synthesis and superconductivity in yttrium-cerium hydrides at high pressures. *Nat Commun* **15**, 1809 (2024).
42. Cao, Z.-Y. *et al.* Probing superconducting gap in CeH<sub>9</sub> under pressure. *ArXiv* <http://arxiv.org/abs/2401.12682> (2024).
43. Ma, C. *et al.* Hydrogen-Vacancy-Induced Stable Superconducting Niobium Hydride at High Pressure. *J Am Chem Soc* **147**, 11028–11035 (2025).
44. Racioppi, S. & Zurek, E. Quantum Effects or Theoretical Artifacts? A Computational Reanalysis of Hydrogen at High-Pressure. *ArXiv* <http://arxiv.org/abs/2510.02098> (2025).

45. Ma, L. *et al.* High Pressure Superconducting transition in Dihydride BiH<sub>2</sub> with Bismuth Open-Channel Framework. *Phys Rev Lett* <https://doi.org/10.1103/kjnw-n6ds> (2025) doi:10.1103/kjnw-n6ds.
46. Song, Y. *et al.* Room-Temperature Superconductivity at 298 K in Ternary La-Sc-H System at High-pressure Conditions. *ArXiv* <http://arxiv.org/abs/2510.01273> (2025).
47. Du, F. *et al.* Tunneling Spectroscopy at Megabar Pressures: Determination of the Superconducting Gap in Sulfur. *Phys Rev Lett* **133**, 036002 (2024).
48. Du, F. *et al.* Superconducting gap of H<sub>3</sub>S measured by tunnelling spectroscopy. *Nature* **641**, 619–624 (2025).
49. Bhattacharyya, P. *et al.* Imaging the Meissner effect in hydride superconductors using quantum sensors. *Nature* **627**, 73–79 (2024).
50. Marathamkottil, A. H. M. *et al.* X-ray Diffraction and Electrical Transport Imaging of Superconducting Superhydride (La,Y)H<sub>10</sub>. (2025).
51. Liu, L. *et al.* Evidence for the Meissner Effect in the Nickelate Superconductor  $\text{La}_{\text{3}}\text{Ni}_2\text{O}_7\delta$  Single Crystal Using Diamond Quantum Sensors. *Phys Rev Lett* **135**, 096001 (2025).
52. Ku, C. *et al.* Point-contact Andreev reflection spectroscopy of layered superconductors with device-integrated diamond anvil cells. *Review of Scientific Instruments* **96**, (2025).
53. Rietwyk, K. J. *et al.* Practical limits to spatial resolution of magnetic imaging with a quantum diamond microscope. *AVS Quantum Science* **6**, (2024).
54. Chen, Y. *et al.* Imaging magnetic flux trapping in lanthanum hydride using diamond quantum sensors. *ArXiv* <http://arxiv.org/abs/2510.21877> (2025).
55. Eremets, M. I., Minkov, V. S., Drozdov, A. P. & Kong, P. P. The characterization of superconductivity under high pressure. *Nat Mater* **23**, 26–27 (2024).
56. Minkov, V. S., Ksenofontov, V., Bud'ko, S. L., Talantsev, E. F. & Eremets, M. I. Magnetic flux trapping in hydrogen-rich high-temperature superconductors. *Nat Phys* **19**, 1293–1300 (2023).
57. Minkov, V. S. *et al.* Revaluation of the lower critical field in superconducting H<sub>3</sub>S and LaH<sub>10</sub> (Nature Comm. 13, 3194, 2022). <http://arxiv.org/abs/2408.12675> (2024).
58. Minkov, V. S. *et al.* Magnetic field screening in hydrogen-rich high-temperature superconductors. *Nat Commun* **13**, 3194 (2022).
59. Hao, Q. *et al.* Diamond quantum sensing at record high pressure up to 240 GPa. *ArXiv* <http://arxiv.org/abs/2510.26605> (2025).

60. Cerqueira, T. F. T., Fang, Y., Errea, I., Sanna, A. & Marques, M. A. L. Searching Materials Space for Hydride Superconductors at Ambient Pressure. *Adv Funct Mater* **34**, (2024).
61. Wei, X. *et al.* Design of High-  $T_c$  Quaternary Hydrides Under Moderate Pressures Through Substitutional Doping. *Adv Funct Mater* **35**, (2025).
62. Jiang, Q. *et al.* Prediction of Room-Temperature Superconductivity in Quasi-Atomic  $H_2$ -Type Hydrides at High Pressure. *Advanced Science* **11**, (2024).
63. Belli, F., Torres, S., Contreras-García, J. & Zurek, E. Refining  $T_c$  Prediction in Hydrides via Symbolic-Regression-Enhanced Electron-Localization-Function-Based Descriptors. *Ann Phys* <https://doi.org/10.1002/andp.202500280> (2025) doi:10.1002/andp.202500280.
64. Hansen, M. F. *et al.* Synthesis of  $Mg_2IrH_5$  : A potential pathway to high- $T_c$  hydride superconductivity at ambient pressure. *Phys Rev B* **110**, 214513 (2024).
65. Rastkhadiv, M. A. Revisiting  $YH_9$  Superconductivity and Predicting High- $T_c$  in  $GdYH_5$ . *ArXiv* <http://arxiv.org/abs/2510.10720> (2025).
66. Mishra, S. B. & Margine, E. R. Nonadiabatic and anharmonic effects in high-pressure  $H_3S$  and  $D_3S$  superconductors. *ArXiv* <http://arxiv.org/abs/2510.25902> (2025).
67. Talantsev, E. F. Primary Superconducting Parameters of Highly Compressed Nonclathrate Ternary Hydride  $LaB_2H_8$ . *Physics of Metals and Metallography* **126**, 493–500 (2025).
68. Minkov, V. S. *et al.* Long-Term Stability of Superconducting Metal Superhydrides. <http://arxiv.org/abs/2507.08009> (2025).
69. Talantsev, E. F. Structural and superconducting parameters of highly compressed  $H_3S$ . *SSRN Preprint* at <https://doi.org/10.2139/ssrn.5280053> (2025).
70. Wrona, I. A., Niegodajew, P. & Durajski, A. P. A recipe for an effective selection of promising candidates for high-temperature superconductors among binary hydrides. *Materials Today Physics* **46**, 101499 (2024).
71. Liu, S. *et al.* High-Throughput Study of Ambient-Pressure High-Temperature Superconductivity in Ductile Few-Hydrogen Metal-Bonded Perovskites. *Adv Funct Mater* **34**, (2024).
72. Huang, H. *et al.* High-Temperature Superconductivity of Thermodynamically Stable Fluorite-Type Hydrides at Ambient Pressure. *Advanced Science* <https://doi.org/10.1002/advs.202512696> (2025) doi:10.1002/advs.202512696.
73. Ksenofontov, V., Minkov, V. S., Drozdov, A. P., Pöschl, U. & Erements, M. I. Signs of Possible High-Temperature Superconductivity in Graphite Intercalated with Lithium-Based Alloys. *ArXiv* <http://arxiv.org/abs/2510.03256> (2025).
74. McMillan, W. L. Transition Temperature of Strong-Coupled Superconductors. *Physical Review* **167**, 331–344 (1968).

75. Dynes, R. C. McMillan's equation and the  $T_c$  of superconductors. *Solid State Commun* **10**, 615–618 (1972).
76. Talantsev, E. F. Advanced McMillan's equation and its application for the analysis of highly-compressed superconductors. *Supercond Sci Technol* **33**, 094009 (2020).
77. Talantsev, E. F. & Stolze, K. Resistive transition of hydrogen-rich superconductors. *Supercond Sci Technol* **34**, 064001 (2021).
78. Talantsev, E. F. The electron–phonon coupling constant and the Debye temperature in polyhydrides of thorium, hexadeuteride of yttrium, and metallic hydrogen phase III. *J Appl Phys* **130**, 195901 (2021).
79. Errea, I. Superconducting hydrides on a quantum landscape. *Journal of Physics: Condensed Matter* **34**, 231501 (2022).
80. Pickard, C. J., Errea, I. & Eremets, M. I. Superconducting Hydrides Under Pressure. *Annu Rev Condens Matter Phys* **11**, 57–76 (2020).
81. Errea, I. *et al.* High-Pressure Hydrogen Sulfide from First Principles: A Strongly Anharmonic Phonon-Mediated Superconductor. *Phys Rev Lett* **114**, 157004 (2015).
82. Errea, I. *et al.* Quantum hydrogen-bond symmetrization in the superconducting hydrogen sulfide system. *Nature* **532**, 81–84 (2016).
83. Errea, I. *et al.* Quantum crystal structure in the 250-kelvin superconducting lanthanum hydride. *Nature* **578**, 66–69 (2020).
84. Gao, K. *et al.* The Maximum  $T_c$  of Conventional Superconductors at Ambient Pressure. <http://arxiv.org/abs/2502.18281> (2025).
85. Pallecchi, I. *et al.* Experimental investigation of electronic interactions in collapsed and uncollapsed  $\text{LaFeAsO}_{2-x}$  phases. *Phys Rev B* **108**, 014512 (2023).
86. Yang, K. *et al.* Charge fluctuations above  $T_{CDW}$  revealed by glasslike thermal transport in kagome metals  $\text{AVSb}_5$  ( $A = \text{Rb, Cs}$ ). *Phys Rev B* **107**, 184506 (2023).
87. Poole, C. P., Farach, H., Creswick, R. & Prozorov, R. *Superconductivity*. (Academic Press, London, UK, 2007).
88. Ni, D. *et al.* Layered polymorph of titanium triiodide. *Phys Rev Mater* **6**, 124001 (2022).
89. Bouquet, F. *et al.* Phenomenological two-gap model for the specific heat of  $\text{MgB}_2$ . *Europhysics Letters (EPL)* **56**, 856–862 (2001).



90. Wälti, Ch. *et al.* Strong electron-phonon coupling in superconducting  $\text{MgB}_2$  A specific heat study. *Phys Rev B* **64**, 172515 (2001).
91. Wang, A. *et al.* Magnetic mixed valent semimetal  $\text{EuZnSb}_2$  with Dirac states in the band structure. *Phys Rev Res* **2**, 033462 (2020).
92. Shang, T. *et al.* Enhanced  $T_c$  and multiband superconductivity in the fully-gapped  $\text{ReBe}_{22}$  superconductor. *New J Phys* **21**, 073034 (2019).
93. Bloch, F. Zum elektrischen Widerstandsgesetz bei tiefen Temperaturen. *Zeitschrift für Physik* **59**, 208–214 (1930).
94. Grüneisen, E. Die Abhängigkeit des elektrischen Widerstandes reiner Metalle von der Temperatur. *Ann Phys* **408**, 530–540 (1933).
95. Talantsev, E. F. An approach to identifying unconventional superconductivity in highly-compressed superconductors. *Supercond Sci Technol* **33**, 124001 (2020).
96. Talantsev, E. F. The dominance of non-electron–phonon charge carrier interaction in highly-compressed superhydrides. *Supercond Sci Technol* **34**, 115001 (2021).
97. Klimczuk, T., Królak, S. & Cava, R. J. Superconductivity of Ta–Hf and Ta–Zr alloys: Potential alloys for use in superconducting devices. *Phys Rev Mater* **7**, 064802 (2023).
98. Ma, K. *et al.* Superconductivity with High Upper Critical Field in the Cubic Centrosymmetric  $\eta$ -Carbide  $\text{Nb}_4\text{Rh}_2\text{C}_{1-6}$ . *ACS Materials Au* **1**, 55–61 (2021).
99. Jonas, D. G. C., Biswas, P. K., Hillier, A. D., Mayoh, D. A. & Lees, M. R. Quantum muon diffusion and the preservation of time-reversal symmetry in the superconducting state of type-I rhenium. *Phys Rev B* **105**, L020503 (2022).
100. Hu, Z. *et al.* Robust three-dimensional type-II Dirac semimetal state in  $\text{SrAgBi}$ . *NPJ Quantum Mater* **8**, 20 (2023).
101. Susner, M. A., Bhatia, M., Sumption, M. D. & Collings, E. W. Electrical resistivity, Debye temperature, and connectivity in heavily doped bulk  $\text{MgB}_2$  superconductors. *J Appl Phys* **105**, (2009).
102. Putti, M. *et al.* Electron transport properties of  $\text{MgB}_2$  in the normal state. *Eur Phys J B* **25**, 439–443 (2002).
103. Jiang, H. *et al.* Physical properties and electronic structure of  $\text{Sr}_2\text{Cr}_3\text{As}_2\text{O}_{10}$  containing  $\text{CrO}_2$  and  $\text{Cr}_2\text{O}_3$

- $\text{As}_2$  square-planar lattices. *Phys Rev B* **92**, 205107 (2015).
104. Wiesmann, H. *et al.* Simple Model for Characterizing the Electrical Resistivity in  $\text{As}_{15}$  Superconductors. *Phys Rev Lett* **38**, 782–785 (1977).
  105. Varshney, D. Impurity, phonon and electron contributions to the electrical resistivity of single-crystal  $\text{MgB}_2$ . *Supercond Sci Technol* **19**, 685–694 (2006).
  106. Cooper, J. R. Electrical resistivity of an Einstein solid. *Phys Rev B* **9**, 2778–2780 (1974).
  107. Pinsook, U. & Tanthum, P. Universal resistivity from electron-phonon interaction based on Einstein model: Application to near-room temperature superconductors. *Next Materials* **6**, 100302 (2025).
  108. Xie, Y. *et al.* The defect level and ideal thermal conductivity of graphene uncovered by residual thermal reffusivity at the 0 K limit. *Nanoscale* **7**, 10101–10110 (2015).
  109. Ren, X.-X., Kang, W., Cheng, Z.-F. & Zheng, R.-L. Temperature-Dependent Debye Temperature and Specific Capacity of Graphene. *Chinese Physics Letters* **33**, 126501 (2016).
  110. Pop, E., Varshney, V. & Roy, A. K. Thermal properties of graphene: Fundamentals and applications. *MRS Bull* **37**, 1273–1281 (2012).
  111. Tewary, V. K. & Yang, B. Singular behavior of the Debye-Waller factor of graphene. *Phys Rev B* **79**, 125416 (2009).
  112. Moreh, R., Shnig, N. & Zabel, H. Effective and Debye temperatures of alkali-metal atoms in graphite intercalation compounds. *Phys Rev B* **44**, 1311–1317 (1991).
  113. Allen, P. B. & Dynes, R. C. Transition temperature of strong-coupled superconductors reanalyzed. *Phys Rev B* **12**, 905–922 (1975).
  114. Semenok, D. Computational design of new superconducting materials and their targeted experimental synthesis. *PhD Thesis; Skolkovo Institute of Science and Technology* <https://doi.org/10.13140/RG.2.2.28212.12161> (2023) doi:10.13140/RG.2.2.28212.12161.
  115. Bardeen, J., Cooper, L. N. & Schrieffer, J. R. Theory of Superconductivity. *Physical Review* **108**, 1175–1204 (1957).
  116. G. M. Eliashberg. Interactions between Electrons and Lattice Vibrations in a Superconductor. *Sov. Phys.–JETP* **11**, 696 (1960).
  117. Riley, G. N., Malozemoff, A. P., Li, Q., Fleshler, S. & Holesinger, T. G. The freeway model: New concepts in understanding supercurrent transport in Bi-2223 tapes. *JOM* **49**, 24–27 (1997).
  118. Nadifi, H. *et al.* Superconductive percolation in Bi-based superconductor/Bi-based insulator composites: case of Bi-2223/Bi-2310 and Bi-2212/BiFeO<sub>3</sub>. *Supercond Sci Technol* **13**, 1174–1179 (2000).

119. Yeshurun, Y., Malozemoff, A. P. & Shaulov, A. Magnetic relaxation in high-temperature superconductors. *Rev Mod Phys* **68**, 911–949 (1996).
120. McElfresh, M. W., Yeshurun, Y., Malozemoff, A. P. & Holtzberg, F. Remanent magnetization, lower critical fields and surface barriers in an YBa<sub>2</sub>Cu<sub>3</sub>O<sub>7</sub> crystal. *Physica A: Statistical Mechanics and its Applications* **168**, 308–318 (1990).
121. Eley, S., Miura, M., Maiorov, B. & Civale, L. Universal lower limit on vortex creep in superconductors. *Nat Mater* **16**, 409–413 (2017).
122. MCHENRY, M. & SUTTON, R. Flux pinning and dissipation in high temperature oxide superconductors. *Prog Mater Sci* **38**, 159–310 (1994).
123. Maley, M. P., Willis, J. O., Lessure, H. & McHenry, M. E. Dependence of flux-creep activation energy upon current density in grain-aligned YBa<sub>2</sub>Cu<sub>3</sub>O<sub>7-x</sub>. *Phys Rev B* **42**, 2639–2642 (1990).
124. Eley, S., Willa, R., Chan, M. K., Bauer, E. D. & Civale, L. Vortex phases and glassy dynamics in the highly anisotropic superconductor HgBa<sub>2</sub>CuO<sub>4+δ</sub>. *Sci Rep* **10**, 10239 (2020).
125. Cole, H. M. *et al.* Plastic vortex creep and dimensional crossovers in the highly anisotropic superconductor  $\text{HgBa}_2\text{CuO}_{4+x}$ . *Phys Rev B* **107**, 104509 (2023).
126. Iida, K., Hänisch, J. & Tarantini, C. Fe-based superconducting thin films on metallic substrates: Growth, characteristics, and relevant properties. *Appl Phys Rev* **5**, 031304 (2018).